

Supporting information

Transformation of native, nanoscale and ionic Cu and Zn during the incineration of digested sewage sludge (biosolids)

Jonas Wielinski^{1,2}, Alexander Gogos¹, Andreas Voegelin¹, Christoph Müller³, Eberhard Morgenroth^{1,2}, Ralf Kaegi^{1,*}

¹ Eawag, Swiss Federal Institute of Aquatic Science and Technology, 8600 Dübendorf, Switzerland

² ETH Zürich, Institute of Environmental Engineering, 8093 Zürich, Switzerland

³ ETH Zürich, Institute of Energy Technology, 8092 Zürich, Switzerland

*Corresponding author: Ralf Kaegi¹, ralf.kaegi@eawag.ch, Eawag, Überlandstrasse 133, 8600 Dübendorf, Switzerland.

This Supporting information contains: 31 pages,
14 figures,
11 tables.

S1. Detailed information on the pilot fluidized bed reactor

The bubbling bed type pilot FBR consists of an incineration unit (heater, reactor, sludge feed) and an off gas unit (heat exchanger, two electrostatic precipitators (ESPs), ash bin) (Figure S1 and Figure S2). A mass flow controller (red-y, Voegtlin, Switzerland) was used to adjust the gas flow between 50 and 200 L_n/min (norm liter per minute). In case of power failure, a fail open (F.O.) magnetic valve was triggered and an air flow of 120 L_n/min was supplied by an external air compressor to prevent an overheating of the incinerator. The incoming air was heated by a 15 kW electric resistance heater (LE 10000 DF-R HT, Leister, Switzerland) and passed the windbox and a distributor plate ($d = 10$ cm) with 120 evenly distributed holes ($d = 1$ mm). The pressure in the windbox beneath the distributor plate was approximately 1.45 kPa above atmospheric pressure. The sand bed ($h = 5$ cm, $w = 0.7$ kg, $630 > d_{\text{sand}} > 800$ μm) above the distributor plate was fluidized at bubbling bed type conventional fluidization conditions.¹⁻² The bed was composed of Geldart group B solids³⁻⁴ with a theoretical minimal fluidization occurring at a 0.9 kPa pressure drop¹. Typical operation conditions were $T_{\text{sand bed}} \approx 820 - 840$ °C and air flow ≈ 120 L_n/min leading to a fluidization with a dimensionless gas velocity $u^* = 0.38$ and a dimensionless particle diameter $d^* = 11.75$ (conventional fluidization conditions).¹ Under typical bed loadings the pressure above the sand bed was approximately 0.35 kPa above atmospheric pressure, thus a pressure drop of 1.1 kPa occurs. Dried sludge was continuously fed via a spiral conveyor 20 cm above the fluidized bed at rates of 0.8 kg/h. The added sludge particles devolatilized immediately after being added to the hot sand bed. Water vapor, volatile hydrocarbons, other gases (e.g. CO₂, CO) and small ash particles were transported upwards and the hydrocarbons burned in the reactor column. The reactor (or freeboard) temperature fluctuated between 400 and 800 °C, depending on the sludge load in the fluidized bed. The reactor pressure was held constantly at -1.6 kPa by a draught fan at the end of the off gas unit. A lambda sensor monitored residual oxygen concentrations and CO equivalents (COe) at the upper end of the reactor column. Residual oxygen concentration depended on the fuel load in the bed and typically varied between 12% and 16%. COe was usually below 100 ppm, depending on the temperature in the sand bed and reactor. Higher temperatures in the sand bed and the reactor lead to lower values of COe. A heat

exchanger, installed at the upper end of the reactor reduced the off gas temperature to 110 °C. The off gas was further fed into the first of two identical electrostatic precipitators (ESPs) (OekoTube-Inside, Oekosolve, Switzerland). A flexible resistance heater was wrapped around each ESP to keep the temperature above the dew point. Particles passing the ESP units were collected in a filter bag at the end of the off gas stream. After an experiment, the ESP units were agitated and the particles collected from the ash bin.

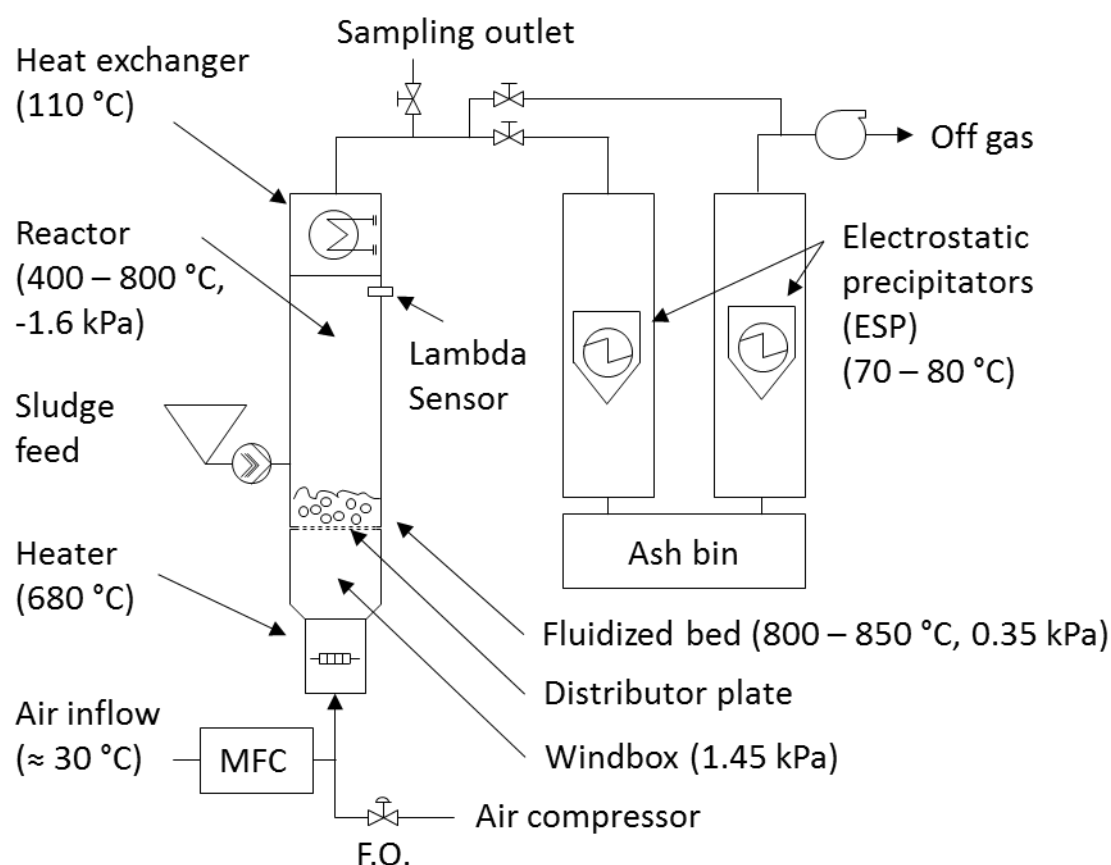


Figure S1: Schematic of the bubbling bed type pilot fluidized bed reactor. The temperatures describe the gas temperatures in the respective part of the incinerator measured by several thermo elements.



Figure S2: Image of the pilot scale FB incinerator. The aluminum case has extensions of 1.55 m x 1.05 m x 2.25 m (width, depth, height).

S2. Electron micrographs and XRD spectra of CuO and ZnO-NP

61 **Sample preparation for TEM analyses:**

62 The prepared ENP dispersions were diluted 1:500 in 0.2% NovaChem and bath sonicated for 2 minutes. A
63 thin layer of Parafilm was stretched on the base of an aluminium cone that fitted into a 1.5 mL Eppendorf
64 tube. A Ni base (for CuO-NP) or a Cu base (for ZnO-NP) carbon coated TEM grid was functionalized by
65 floating the TEM grid on a 0.1% poly-L-lysine (Sigma-Aldrich, CH) droplet for 10 min and washed in
66 three drops of DI water (with drying steps using Kimwipe tissues). The functionalized TEM grid was then
67 gently pressed onto the parafilm. The aluminium cones with the TEM grids were inserted into the
68 Eppendorf tubes, filled with 1.0 mL of a diluted dispersion and centrifuged at 14'000 rpm for 60 min.
69 After this, the supernatant was removed, the grid gently removed from the parafilm, washed in three drops
70 of DI water, dried and investigated using Hitachi HT7700 TEM.

71

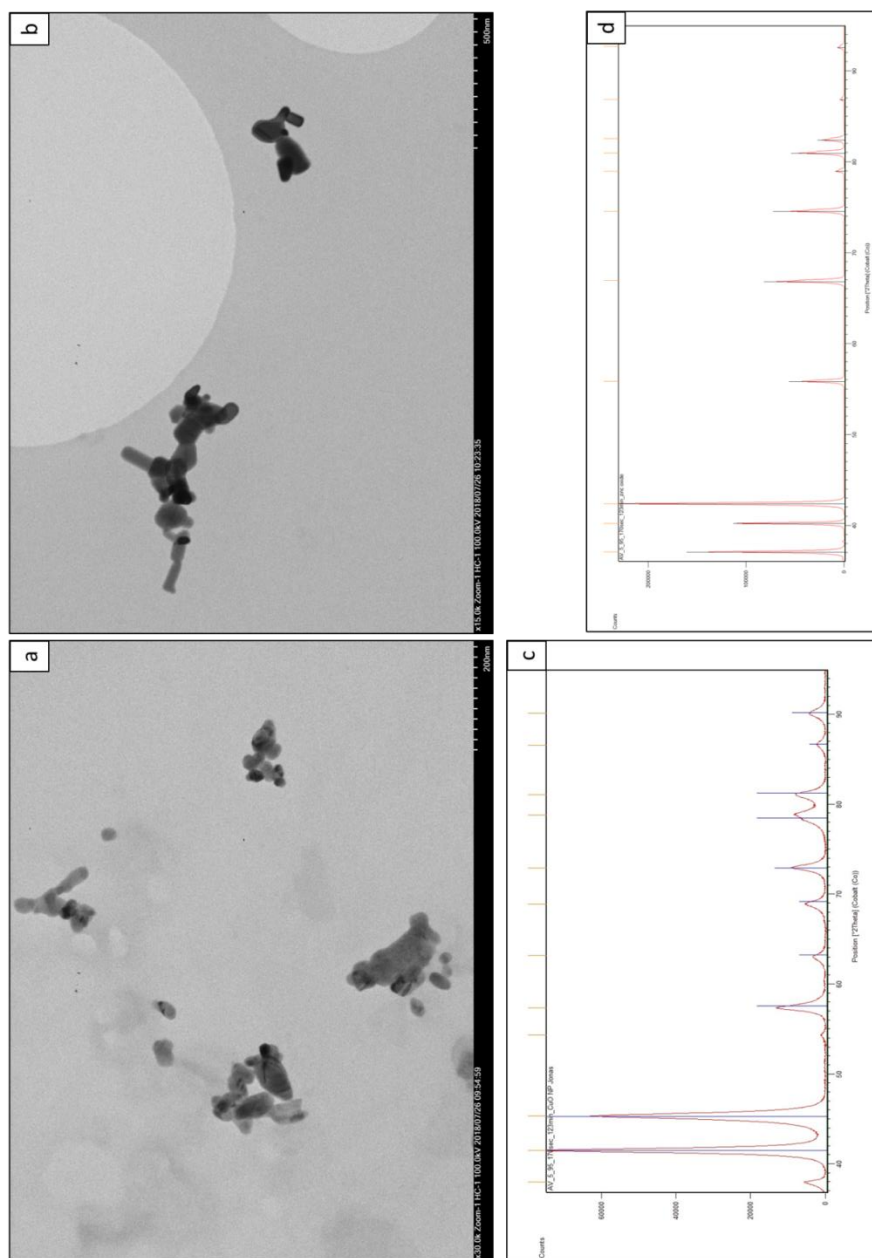


Figure S3: TEM bright field images of the CuO-NP (a) and ZnO-NP (b) used for the spiking experiments. The images were recorded on a Hitachi HT7700 with an acceleration voltage of 100 kV. X-ray powder diffractogram of CuO-NP (c) (red curve) and the peaks assigned to synthetic tenorite (blue spikes) and of ZnO-NP (d) (red curve) and the peaks assigned to synthetic zincite (black spikes).⁵

S3. CuFe_2O_4 synthesis

CuO (tenorite powder 99.995%, Aldrich Chem. Co., USA) and Fe_2O_3 (hematite powder, Standard 85, Bayferrox, USA) were mixed at a stoichiometric ratio of 1 to 1.1 using mortar and pestle. The mixture was added to an Al_2O_3 vessel and reacted at 950 °C for 8 h. The product was removed from the oven after cooling down to room temperature and analyzed using X-ray powder diffraction (XRPD) which indicated the presence of a tetragonally distorted inverse spinel (Figure S4) ⁶. The distortion is a result from the Jahn-Teller effect ⁷. The product from stoichiometric mixture of CuO and Fe_2O_3 had significant amounts of CuO remaining, as indicated by XRPD (results not shown).

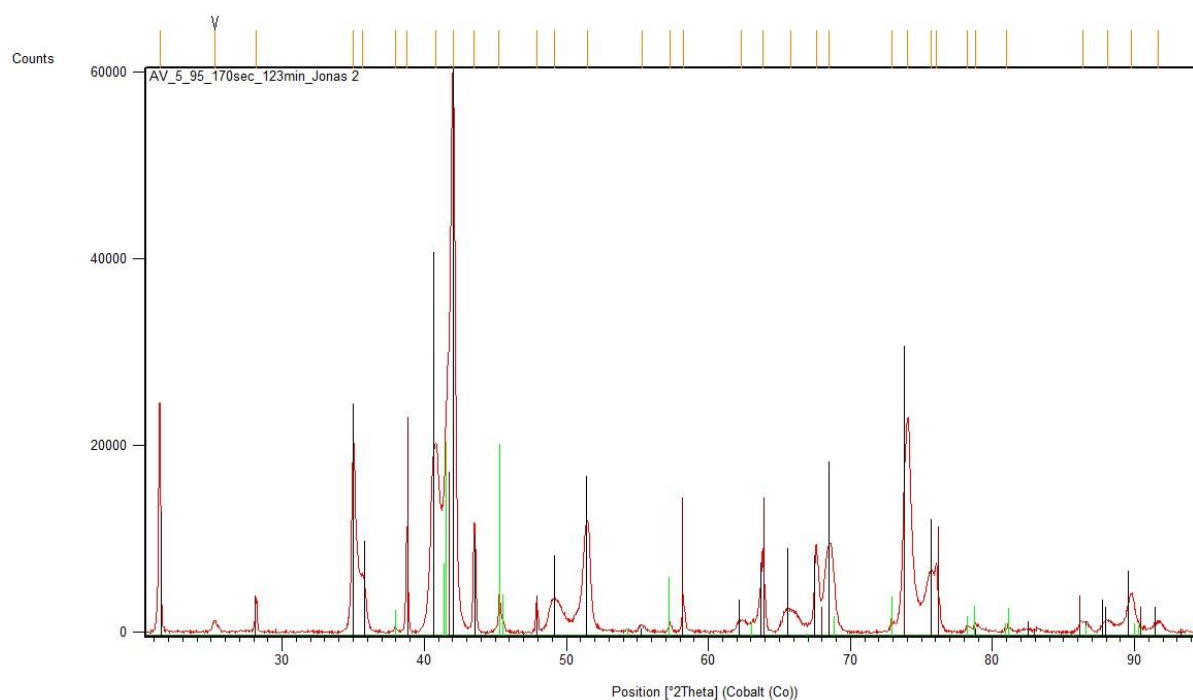


Figure S4: XRPD results of the synthesis of CuFe_2O_4 . The black lines indicate a reference diffractogram of a distorted tetragonal cupro spinel. The green lines indicate a reference diffractogram of hematite.

S4. Detailed results of the sample characterization

Table S1: Carbon content, Cu and Zn concentrations and information of sample origin and incineration of all samples. Cu and Zn concentrations are mean values and standard deviations of three replicate

91 digestions. Cu and Zn concentrations were determined by ICP-MS (Agilent 8900QQQ or Agilent 7500cx)
 92 or ICP-OES. Al and Fe concentrations were determined by ICP-OES for all pristine sludge samples. *Cu
 93 and Zn concentrations were additionally determined by XRF.

Sample name	TC, %	Cu, [mg/kg]	Zn, [mg/kg]	Cu*, [mg/kg]	Zn*, [mg/kg]	Al, [g/kg]	Fe, [g/kg]	Place of incineration	Sampling location
A	25.144	94.5 ± 0.1	524.7 ± 258.3	89.6 ± 0.7	316.6 ± 0.9	16.0 ± 2.7	82.1 ± 4.1	-	WWTP Rhein
A-af	0.169	250.4 ± 2.5	1247.4 ± 5.3	209.6 ± 1.4	1268.6 ± 3			Fluidized bed incineration plant, ARA Rhein, Basel	WWTP Rhein
A-ap	3.179	343 ± 0.4	1400.6 ± 36.7	278.5 ± 1.6	1304.9 ± 3			Pilot FBR	Eawag
B	26.357	331.3 ± 10.9	938.6 ± 14.6	357.6 ± 1.3	1022.0 ± 1.9	12.1 ± 0.1	51.0 ± 1.5	-	WWTP Werdhoelzli
B-af	0.057	877.4 ± 4.4	1530.6 ± 11.4	727.9 ± 2.5	1558.5 ± 3			Fluidized bed incinerator, Werdhölzli, Zurich	WWTP Werdhölzli
B-ap	2.221	670 ± 2.2	2374 ± 46.4	476.0 ± 2.4	2191.9 ± 4			Pilot FBR	Eawag
C	34.082	379.6 ± 6.5	724.1 ± 14.5	367.3 ± 1.0	780.8 ± 1.3	28.7 ± 0.8	58.6 ± 0.8	-	WWTP ProRhen
C-af	0.148	1116.9 ± 17.6	3557.9 ± 42.2	937.7 ± 3.1	3268.7 ± 5			Circulating fluidized bed reactor ProRhen, Basel	WWTP ProRhen
C-ap	1.740	1139.1 ± 157.5	3473.7 ± 11	985.1 ± 3.2	3259.6 ± 5			Pilot FBR	Eawag
D	29.325	390.6 ± 1	805.8 ± 39.9			19.1 ± 4.3	48.3 ± 1.3	-	WWTP Winznau
D-NP (Cu)	28.969	1243.6 ± 4	1187.9 ± 95.3					-	WWTP Winznau
D-AQ (Cu)	29.678	1482.8 ± 38.1	718.3 ± 100.3					-	WWTP Winznau
D-NP (Zn)	28.791	389.5 ± 7.6	6238.6 ± 1475					-	WWTP Winznau, Solothurn
D-AQ (Zn)	28.756	388.6 ± 6.9	5285.2 ± 298.4					-	WWTP Winznau
D-ap	1.614	832.3 ± 1.3	2887.6 ± 30.1					Pilot FBR	Eawag
D-NP-	1.769	2735.4	6499.9					Pilot FBR	Eawag

ap (Cu)		± 53.0	± 540						
D-AQ-ap (Cu)	1.208	3011.1 ± 52.5	5211.4 ± 13.4					Pilot FBR	Eawag
D-NP-ap (Zn)	1.500	884.4 \pm 4	14381.6 ± 825.2					Pilot FBR	Eawag
D-AQ-ap (Zn)	1.669	1041.5 ± 8.8	13588.1 ± 447.8					Pilot FBR	Eawag
D-ap (bottom ash)	0.013	539.4 \pm 3.7	2706.4 ± 78					Pilot FBR	Eawag
D-NP-ap (Cu, bottom)	0.010	1481.4 ± 17.2	1571.5 ± 157.4					Pilot FBR	Eawag
D-AQ-ap (Cu, bottom)	0.011	2434.8 ± 94.5	2116.8 ± 479.2					Pilot FBR	Eawag
D-NP-ap (Zn, bottom)	0.016	875.1 \pm 52.5	10553.0 ± 327.9					Pilot FBR	Eawag
D-AQ-ap (Zn, bottom)	0.007	961.9 \pm 10.1	13144.6 ± 670.2					Pilot FBR	Eawag

94

95 **S5. Detailed results of the mass balances**

96 Table S2: Masses of sludge, fly ash, the bed after incineration, ash in the filter bag, the fraction of solids in
97 the sludge, the fraction of combustibles and the recovered mass in per cent. The mass of the sand bed prior
98 to every experiment was 700 g. Samples A-C were used for XAS measurements to compare the
99 performance of the pilot FBR to the full-scale incinerators regarding the speciation of Cu and Zn.

Sample	Sludge incinerated, [kg]	Fly ash, [g]	Bed weight (m_{bed} , [g])	Bottom ash, [g]	Ash in filter bag, [g]	X_{TS} , [-]	X_{ash} , [-]	Recovered mass, %	Recovered Cu, %	Recovered Zn, %
A	0.800	14.6	989.3	289.3	4.35	0.94	0.350	117	N.A.	N.A.
B	1.000	43.6	1062.6	362.6	6.53	0.94	0.443	99	N.A.	N.A.
C	1.000	51.0	975.7	275.7	1.08	0.94	0.319	109	N.A.	N.A.
D	0.700	29.3	945.1	245.1	0.70	0.94	0.402	104	55	114
D-NP (Cu)	0.500	9.6	861.8	161.8	0.00	0.94	0.402	91	47	77
D-AQ (Cu)	0.500	22.0	789.4	89.4	0.70	0.94	0.402	59	65	114
D-NP (Zn)	0.500	13.3	865.2	165.2	1.69	0.94	0.402	95	84	65

D-AQ (Zn)	0.500	15.2	829.3	129.3	4.95	0.94	0.402	79	91	91
--------------	-------	------	-------	-------	------	------	-------	----	----	----

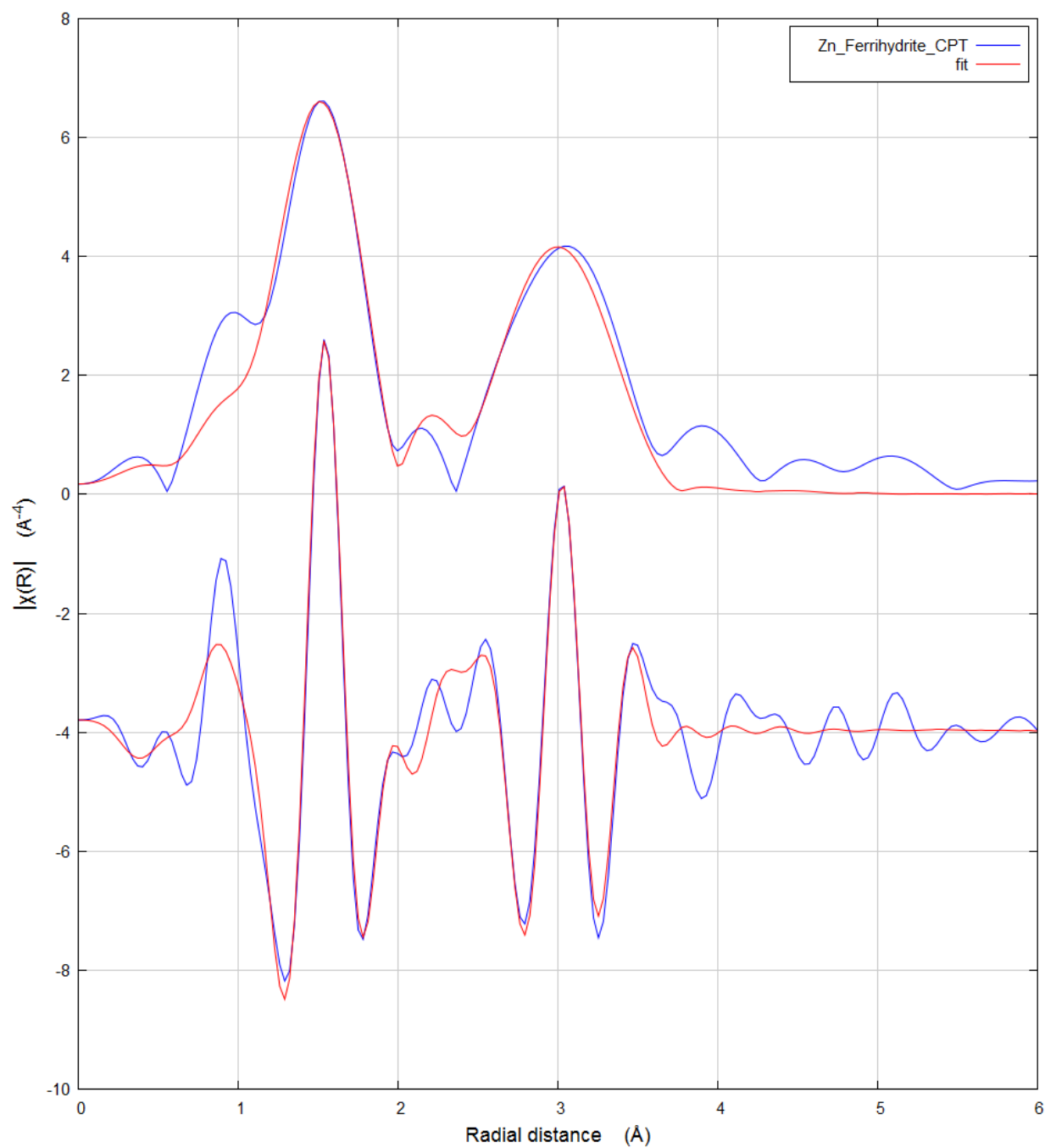
S6. Reference material characterization: Zn-Ferrihydrite co-precipitate (Zn-Fh-CPT)

The reference material ‘Zn-Ferrihydrite-CPT’ has been synthesized and characterized in the scope of a previous project, where it is described as ‘Zn-Ferrihydrite’.⁸ The synthesis in ⁸ was adapted from Schwertmann and Cornell (1991) ⁹. Briefly, Zn-ferrihydrite was precipitated by adding 135 mL 1 M KOH to 75 mL 0.3 M (Fe(NO₃)₃·9 H₂O + Zn(NO₃)₂·4 H₂O) at a molar Zn/(Zn + Fe) ratio of 0.015.⁸⁻⁹ We performed EXAFS shell fitting to further characterize the material. In Athena, a Kaiser-Bessel window was set between k=3 and k=10 with dk=2 and the spectrum was weighted with k³ prior to importing it into the Artemis software code in which the fits were performed.¹⁰ The Zn-Fh-CPT was synthesized as a precursor for goethite ¹¹ and we therefore used the crystallographic data of goethite obtained from the American Mineralogy Database ¹⁰ and substituted the central Fe with Zn. Different scattering paths were evaluated during the fitting process, and the most successful one is presented in Figure S5 and Table S3. The fitting parameters were the shift of the absorption edge energy (ΔE_0), the length, degeneracy and mean square root displacement of each scattering path (Table S3). In our model, Zn is coordinated with oxygen and Fe occupies the second shell. Two single scattering paths, @Zn-O-@Zn and @Zn-Fe-@Zn, where @Zn is the absorber and O and Fe the scatterer described the experimental EXAFS spectrum well (Figure S6 and Figure S7), The Zn - first shell distance of 1.98 Å extracted from the fit to the experimental EXAFS spectrum is consistent with tetrahedrally coordinated Zn ¹², as Zn octahedrally coordinated with oxygen exhibits longer bond distances, e.g. between 2.048 and 2.159 Å as reported for hopeite.¹³ The inter-atomic distances are comparable to those reported for a nanoparticulate ZnFe₂O₄ spinel.¹² Therefore, we conclude that the Zn-Fh-CPT represents Zn incorporated into a weakly crystalline spinel like phase.

123 Table S3: Tabulated shell fitting results. The interatomic distances were fitted as difference to the
 124 reference length as determined by FFEF. For convenience, the actual distance is reported here.

Fit parameter	Evaluated	Type
Amplitude reduction factor	1	Set (not evaluated)
ΔE_0	2.546 ± 3.116	Guess
Degeneracy oxygen (first shell)	4.455 ± 1.639	Guess
Mean square displacement (first shell)	0.00856 ± 0.004396	Guess
Interatomic distance first shell (Zn – O)	1.97631576 ± 0.0233	Guess
Degeneracy iron (second shell)	11.00585 ± 7.44308	Guess
Mean square displacement (second shell)	0.016758 ± 0.00678	Guess
Interatomic distance second shell (Zn – O)	3.4851 ± 0.03428	Guess

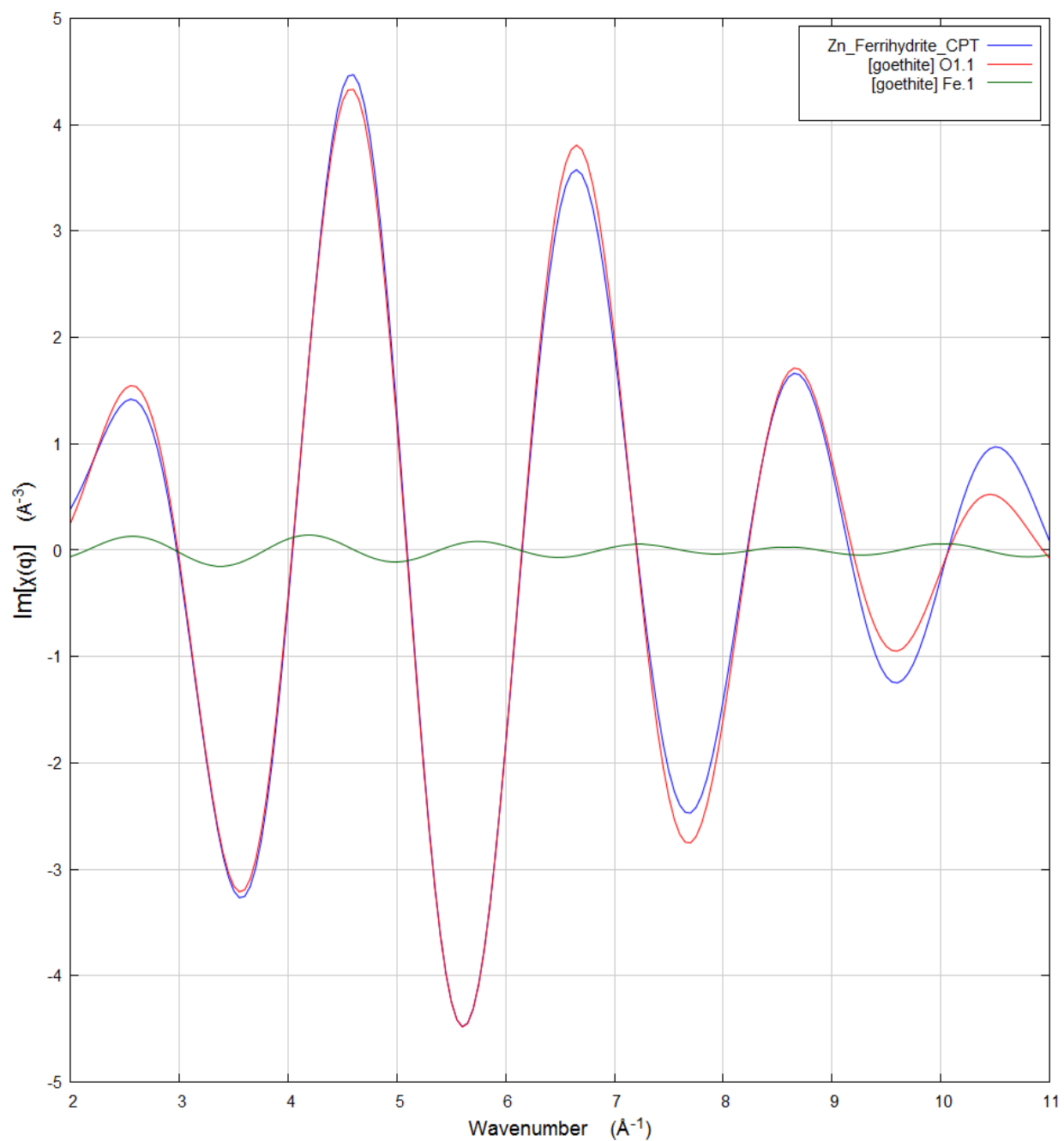
125



126

127 Figure S5: Shell fitting results to the Zn-Ferrihydrite co-precipitate. The upper two lines describe the
 128 magnitude in R-space, the lower two lines the imaginary part in R-space.

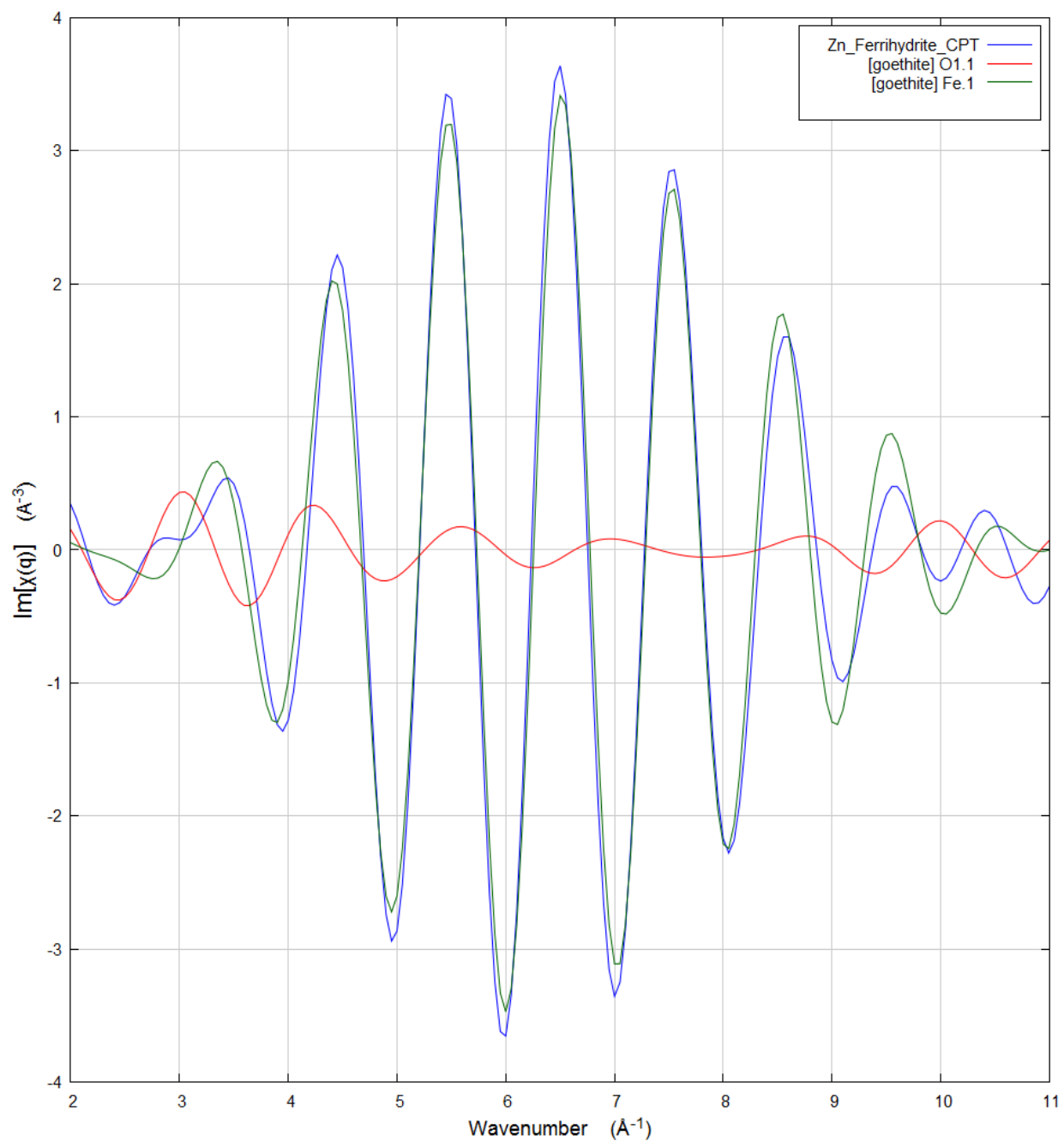
129



130

131 Figure S6: Backward Fourier transform (q-space) of the first shell (oxygen) between $R=0.9 \text{ \AA}$ and $R=2.2$

132 A.



133

134 Figure S7: Backward Fourier transform (q-space) of the second shell (iron) between $R=2.2$ Å and $R=3.8$

135 A.

S7. Comparability between the bottom ash and fly ash speciation

The residual total carbon (TC) content of the pilot fly ashes was slightly higher compared to the fly ashes collected from full-scale incinerators. Higher TC removal rates at constant temperature can be achieved by e.g. longer residence times of the sludge in the fluidized bed.¹⁴ Therefore, the TC content in the experimentally produced bottom ash is considerably lower compared to the experimental fly ash (Table S1). We recorded Cu and Zn XAS spectra of the bottom ash corresponding to C-ap. C-ap was selected due to its high Cu and Zn concentrations.

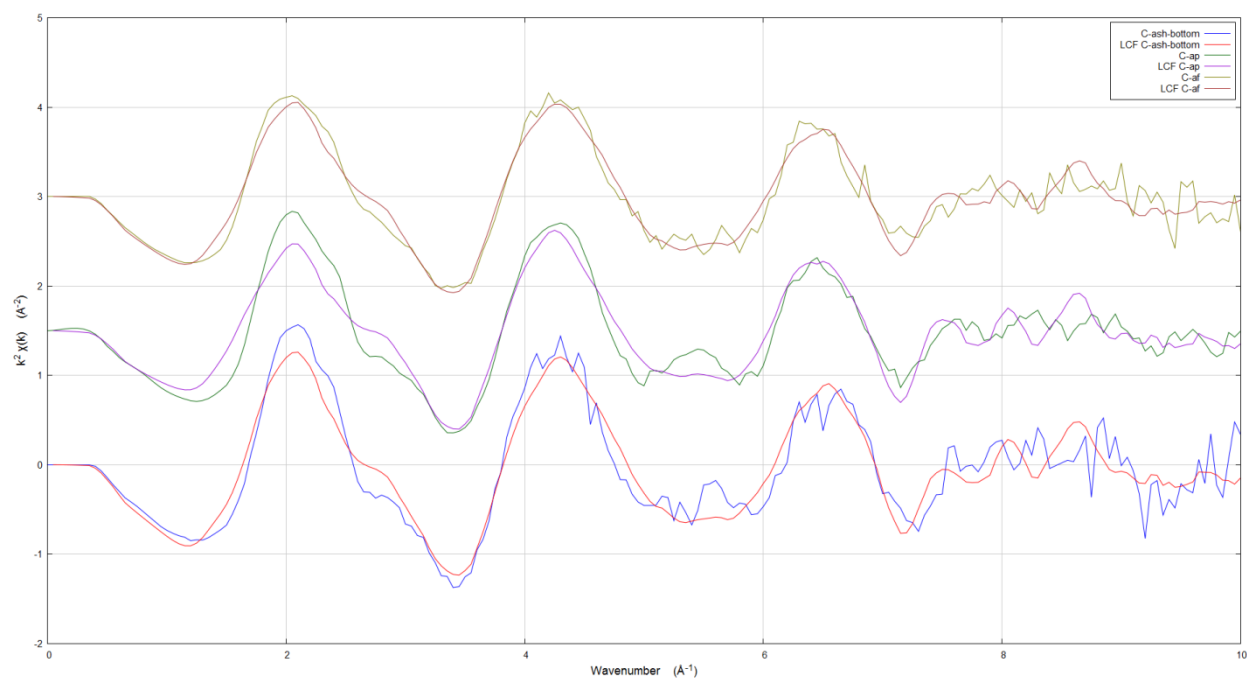
The three most prominent oscillations ($k=3.5$, $k=4.2$ and $k=6.5$) were almost identical in all three samples (Figure S8). Also, the fractions obtained through LCF were comparable within analytical uncertainty (Table S4). We, therefore, conclude that the reduced TC elimination in the pilot ashes compared to the full scale ashes did not affect the behavior / speciation of Cu during the incineration process. The same arguments hold true for Zn, although the spectra for the bottom ash is considerably more noisy limiting the comparison to between 2 – 9 k. (Figure S9). We, therefore conclude, that the less complete elimination of TC did not impact the Cu/Zn speciation and that our pilot FBR mimics the transformation of Cu and Zn in a full scale FBR.

152 Table S4: Cu (upper part) and Zn (lower part) EXAFS LCF fractions for C-ap-bottom ash, C-ap and C-af.

153 The fractions of C-ap and C-af correspond to those in Table S10 and Table S11.

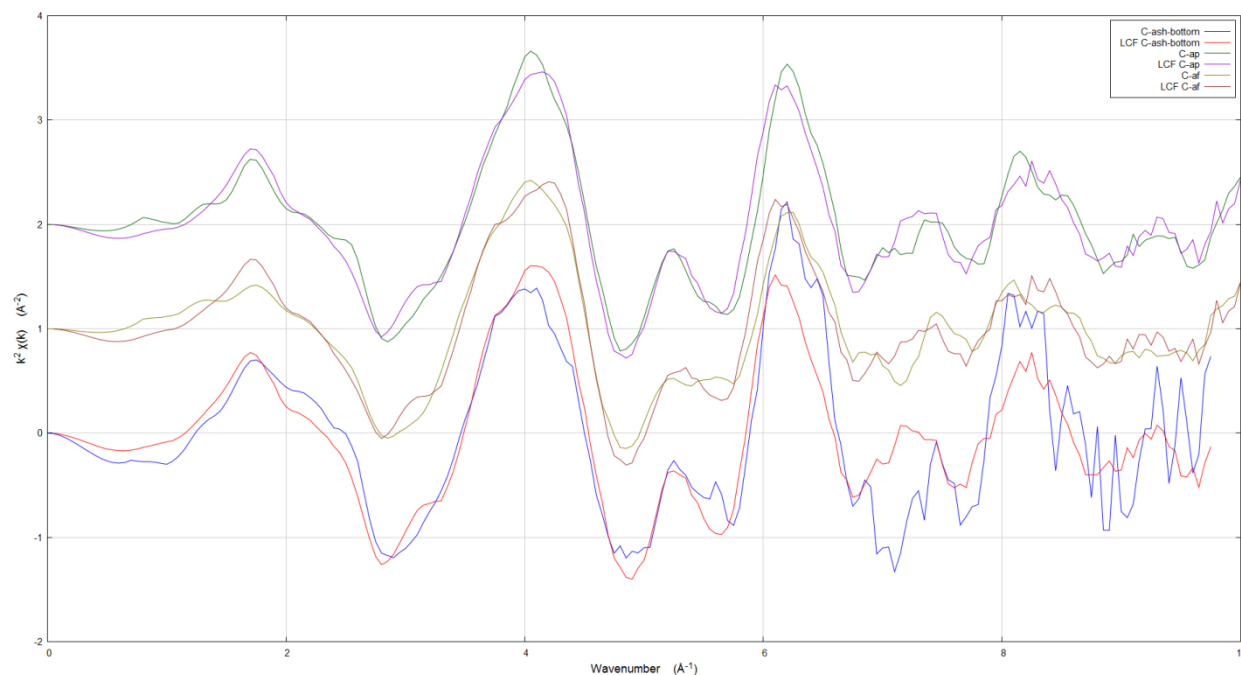
Sample	Cu _x S	CuS	CuO	CuSO ₄	CuFe ₂ O ₄	Cu(II)- acetate	Sum
C-ap- bottom	0.20	0.00	0.36	0.42	0.05	0.00	1.027
C-ap	0.29	0.00	0.32	0.22	0.14	0.00	0.972
C-af	0.24	0.00	0.21	0.30	0.11	0.08	0.965
Sample	ZnS	Zn-Fh- CPT	ZnO	ZnAl ₂ O ₄	Sum		
C-ap- bottom	0.00	1.00	0.07	0.01	1.174		
C-ap	0.00	1.00	0.02	0.00	1.029		
C-af	0.00	0.89	0.09	0.00	0.969		

154



155

156 Figure S8: Cu EXAFS spectra of C-af (green curve), C-ap (red curve) and the bottom ash corresponding
 157 to C-ap (blue curve). Only one scan has been performed for the bottom ash, whereas three scans were
 158 performed for all other samples.



159
 160 Figure S9: Zn EXAFS spectra of C-af (green curve), C-ap (red curve) and the bottom ash corresponding to
 161 C-ap (blue curve). Only one scan has been performed for the bottom ash, whereas three scans were
 162 performed for all other samples.

163 **S8. Identification of major spectral components and suitable reference** 164 **materials**

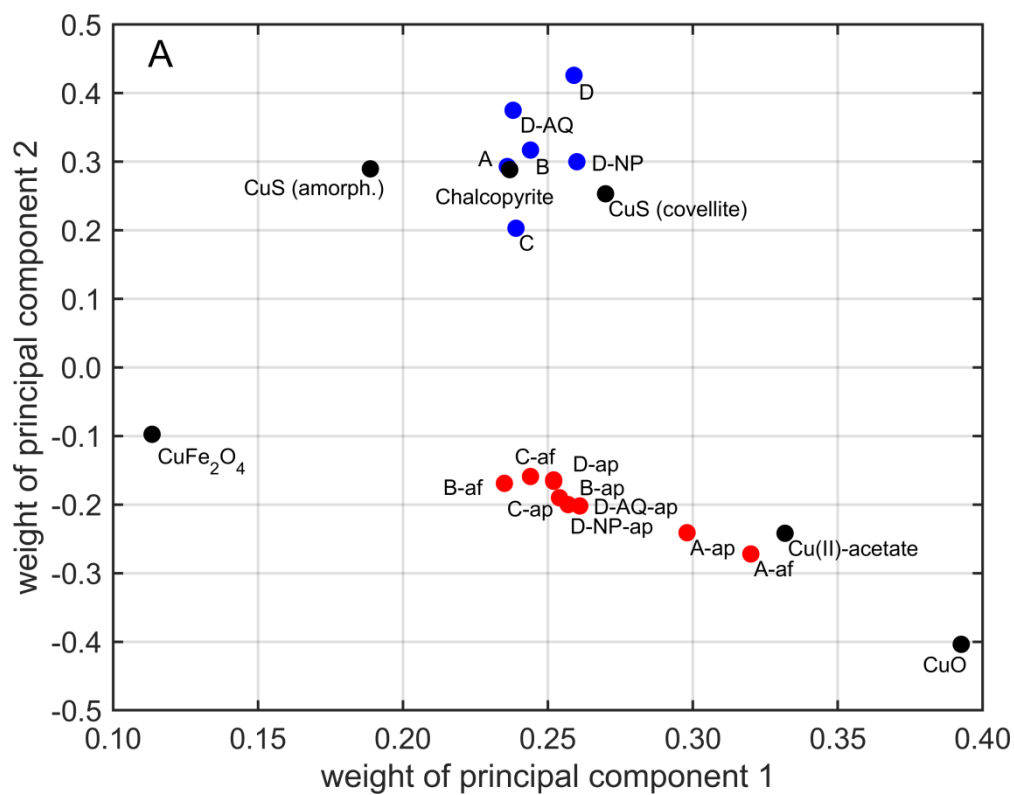
165 Principal component analysis (PCA) was performed to identify the major spectral components of the
 166 experimental Cu and Zn EXAFS spectra. Based on the minimum of the indicator function (IND)¹⁵, six
 167 and five principle components (PCs) were selected to describe the experimental k^2 -weighted Cu and Zn
 168 EXAFS spectra. Suitable spectra from selected reference materials were identified through target testing
 169 (TT).

170 **Cu:** The loadings of the first two PC are presented in Figure S108A. For the sludge samples (blue dots)
 171 the loadings cluster around 0.25 for PC 1 and 0.30 for PC 2. With the exception of the WWTP Rhein
 172 samples, the loadings for PC1 of the ashes (red dots) also scatter around 0.25, but the loadings for PC2 of
 173 around -0.15 are clearly larger compared to the respective loadings of the sludge samples. Therefore, PC 2

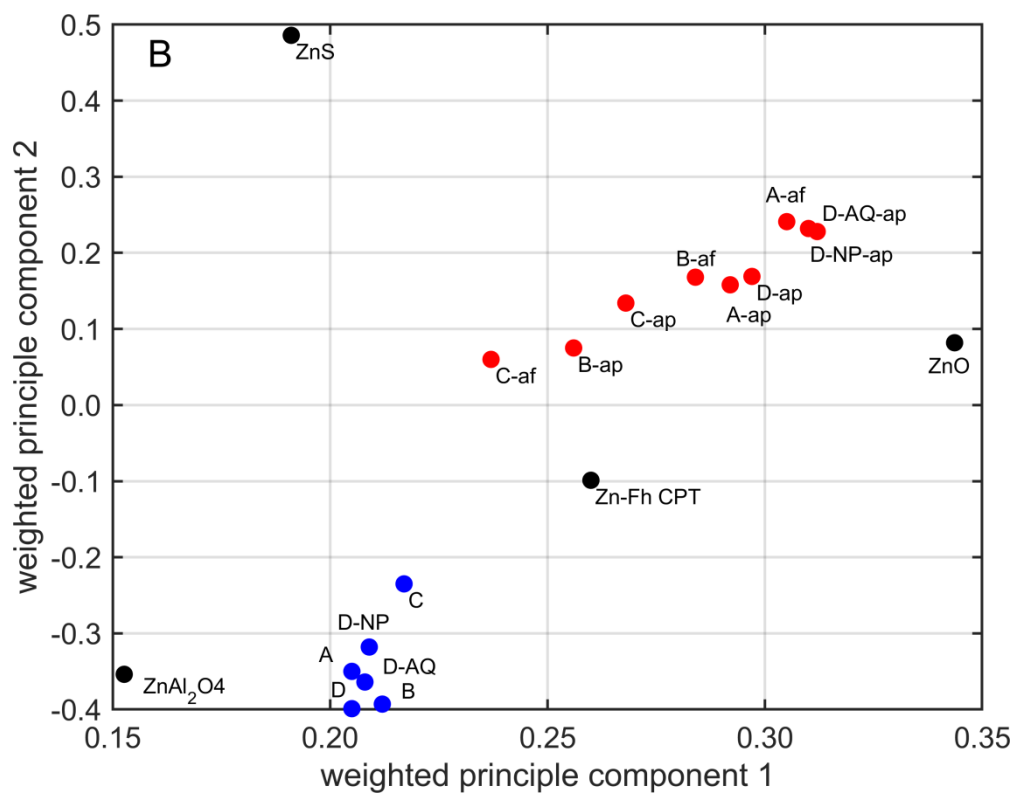
discriminates between sludge and ash samples. Suitable reference compounds required for the reconstruction of the experimental EXAFS spectra were identified through TT using four spectral compounds (Figure S119). Spectra of Cu_xS (amorphous)¹⁶, CuS (covellite), CuFeS_2 (chalcopyrite), CuSO_4 , (copper sulphate), CuO (tenorite), CuFe_2O_4 (cuprospinel) and Cu(II)-acetate yielded SPOIL values between 2.31 and 5.89 and are thus considered as suitable reference spectra. SPOIL values indicate the level of disagreement between the input and the target¹⁷. The reference Cu_xS (amorphous) has been reported as “blue-black” in Patrick et al.¹⁶. The loadings of PC1 and PC2 from the spectra of the sulfur coordinated Cu references (Cu_xS (amorphous), covellite and chalcopyrite) project close to the experimental sludge samples. The loadings of PC1 and PC2 from spectra of oxygen coordinated references (copper sulphate, tenorite, cupro spinel and Cu(II)-acetate) project closer to the loadings of the spectra of the experimental ash samples (Figure S108A, black dots).

Zn: The loadings of PC1 and PC2 of the spectra from the experimental sludge scatter around 0.20 (PC 1) and 0.35 (PC 2) (Figure S108B). The loadings of PC1 and PC2 from the ash spectra are clearly different from respective loadings of the sludge spectra and cluster around 0.3 for PC1 and -0.2 for PC2. TT yielded low SPOIL values (< 8) for ZnS (sphalerite), a Zn-ferrihydrite co-precipitate (Zn-Fh CPT), ZnO (zincite), and ZnAl_2O_4 (gahnite). Franklinite and Zn(II)-acetate had SPOIL values of 13.15 and 32.38. The experimental EXAFS spectra and the spectra from the selected reference materials we successfully reconstructed using four (Cu) and five (Zn) PCs (Figure S119).

The reconstruction of the EXAFS sample and reference material spectra using four (Cu) and five (Zn) PCs proved successful (Figure S119).

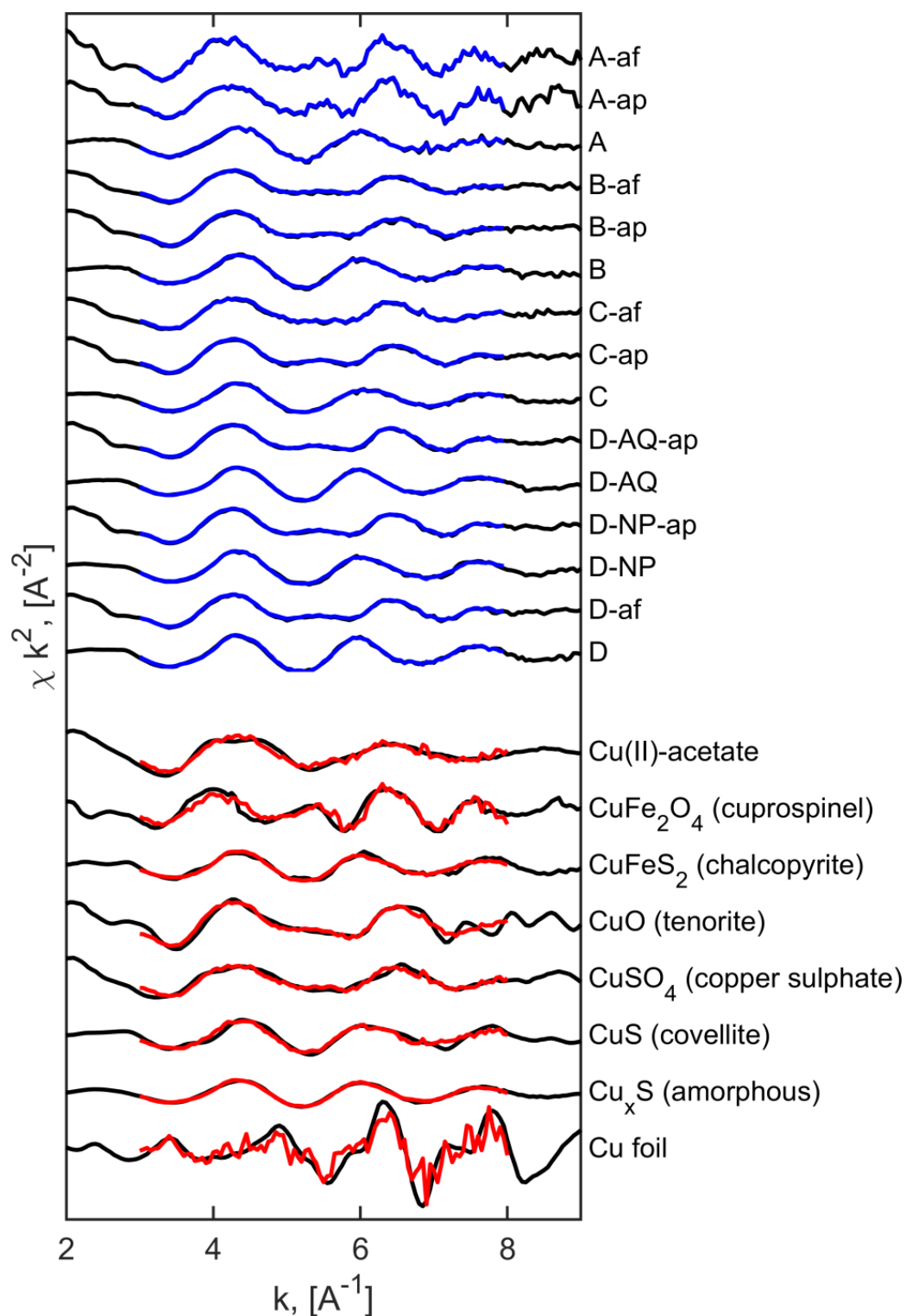


194

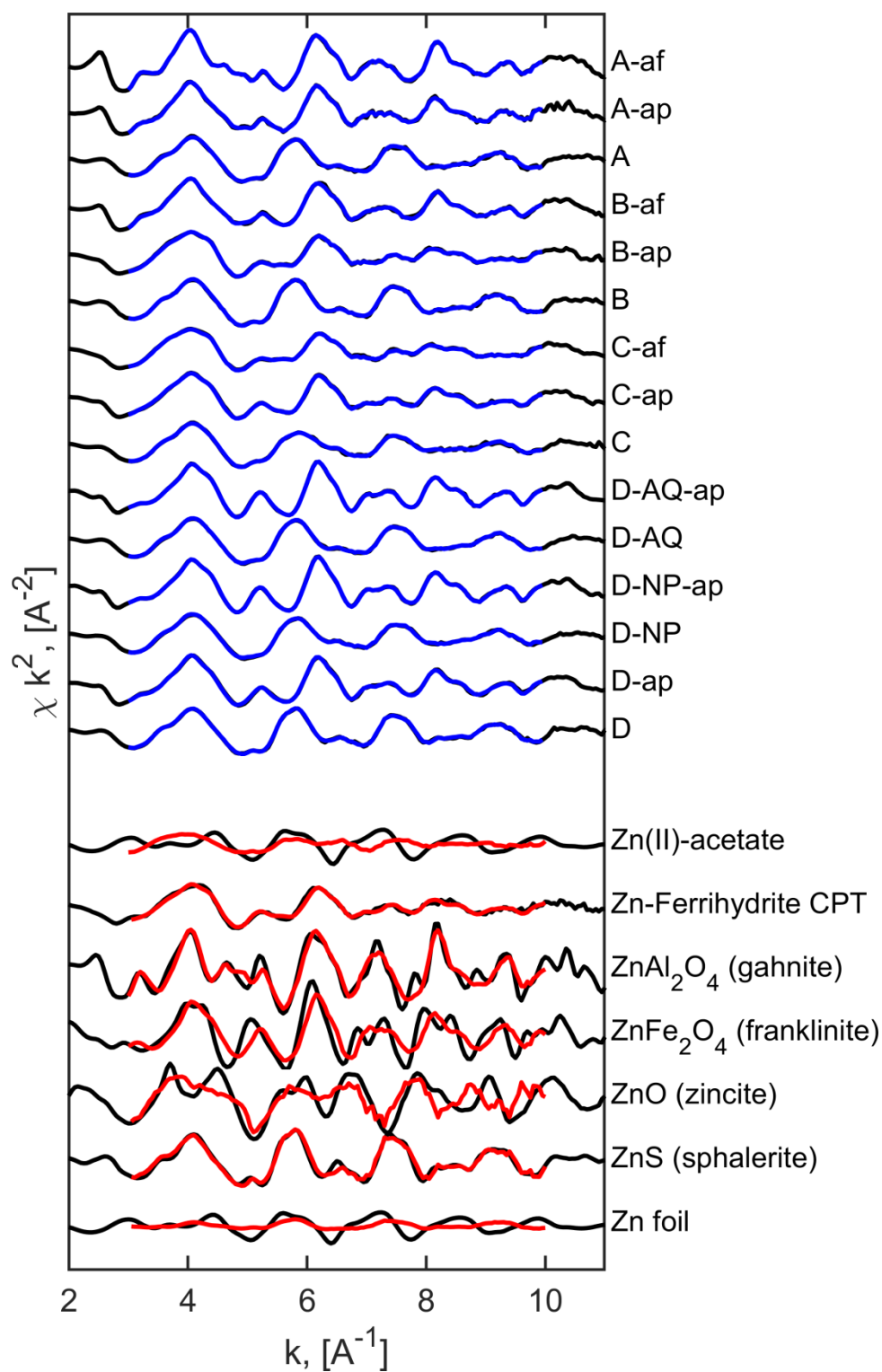


195

196 Figure S10: Loadings of the first versus the second principle component describing the Cu k^2 -weighted
197 EXAFS spectra. The blue dots represent the sludge samples, the red dots represent the ash samples and the
198 black dots represent selected reference materials. Loadings for the experimental spectra were determined
199 using PCA, and loadings for spectra from reference materials were obtained from TT. Only the first two
200 PCs are displayed as they explain 90% of the variance (A). Corresponding information for Zn are given in
201 B. The first two PCs explain 96% of the variance (Table S76).



202
 203 Figure S11: Cu k^2 -weighted EXAFS spectra (black lines). Six spectral PCs were used for the
 204 reconstruction of the sample spectra (blue lines) and for the target testing of the reference materials (red
 205 lines).



206
 207 Figure S12: Zn k^2 -weighted EXAFS spectra (black lines). Six spectral PCs were used for the
 208 reconstruction of the sample spectra (blue lines) and for the target testing of the reference materials (red
 209 lines).

210

211 Table S5: PCA statistics of 15 sludge and ash Cu K-edge k^2 weighted EXAFS ($k = 3 - 9 \text{ \AA}^{-1}$) spectra

212 performed using SIXpack¹⁸.

Compound	Eigenvalue	Variance	Indicator function (IND)
Compound 1	4.10	0.770	0.00127
Compound 2	0.92	0.127	0.00026
Compound 3	0.07	0.027	0.00015
Compound 4	0.03	0.012	9.17e-5
Compound 5	0.02	0.005	7.79 e-5
Compound 6	0.01	0.003	7.40e-5
Compound 7	0.01	0.002	7.93 e-5
...			
Compound 15	0.002	0.000	N.A.

213

214 Table S6: SPOIL values of the reference compounds returned from target testing (TT) of Cu K-edge k^2 -

215 weighted EXAFS reference materials using SIXpack¹⁸. Other reference spectra which were tested

216 included Cu₂O, CuCl₂, Cu(I)-acetate, Cu(II) sorbed on apatite, Cu₂S, Cu(II)-nitrate, CuCO₃, and Cu(I)

217 bound to humic acid. None of them produced reasonable SPOIL values.

Reference compound	SPOIL value	Reference compound	SPOIL value
Cu _x S (amorphous)	2.31	CuO	4.89
CuS	2.68	Cu(II)-acetate	2.91
CuFeS ₂	4.49	Cu foil	1.48
CuSO ₄	3.00	CuFe ₂ O ₄	4.54

219 Table S7: PCA statistics of 15 sludge and ash Zn K-edge weighted with k^2 EXAFS ($k = 3 - 9 \text{ \AA}^{-1}$) spectra
 220 performed using SIXpack¹⁸.

Compound	Eigenvalue	Variance	Indicator function (IND)
Compound 1	5.128	0.714	0.00249
Compound 2	1.827	0.254	0.00022
Compound 3	0.115	0.016	0.00013
Compound 4	0.065	0.009	3.93E-05
Compound 5	0.011	0.001	3.44E-05
Compound 6	0.005	0.001	3.72E-05
...			
Compound 15	0.000	0.000	N.A.

221
 222 Table S8: SPOIL values of the reference compounds returned from target testing (TT) of Zn K-edge k^3 -
 223 weighted EXAFS standards using SIXpack¹⁸. Other reference spectra which were tested included Zn(II)-
 224 nitrate, Zn(II) sorbed on goethite, Zn(II) sorbed on ferrihydrite, hopeite and ZnCO_3 . None of them
 225 produced reasonable SPOIL values.

Reference compound	SPOIL value	Reference compound	SPOIL value
Zn(II)-acetate	32.38	Zn-ferrihydrite CPT	7.90
Zn foil	38.74	ZnO (zincite)	7.22
Gahnite	5.99	ZnS (sphalerite)	2.62
Franklinite	13.15		

226

227

228

S9. EXAFS fitting, quality control parameter and fractions

229

Table S9: Cu and Zn EXAFS LCF quality control parameter.

Sample name	Absorber	Included data points	Variables	R-factor	Chi-square	Reduced chi-square	Sum
A-ap	Cu	121	7	0.212	0.123	14.001	122%
B-ap	Cu	121	7	0.075	0.024	2.787	98%
C-ap	Cu	121	7	0.088	0.029	3.250	97%
A-af	Cu	121	7	0.137	0.083	9.515	126%
B-af	Cu	121	7	0.087	0.024	2.786	88%
C-af	Cu	121	7	0.068	0.021	2.360	96%
A	Cu	121	7	0.067	0.023	2.571	114%
B	Cu	121	7	0.034	0.012	1.400	118%
C	Cu	121	7	0.014	0.004	0.468	110%
D-NP-ap	Cu	121	7	0.095	0.033	3.712	100%
D-AQ-ap	Cu	121	7	0.082	0.027	3.078	100%
D-ap	Cu	121	7	0.076	0.023	2.676	99%
D-NP	Cu	121	7	0.036	0.014	1.599	123%
D-AQ	Cu	121	7	0.027	0.011	1.198	118%
D	Cu	121	7	0.051	0.024	2.787	129%
A-ap	Zn	141	4	0.070	0.040	5.414	107%
B-ap	Zn	141	4	0.043	0.018	2.512	103%
C-ap	Zn	141	4	0.054	0.025	3.491	103%
A-af	Zn	141	4	0.102	0.074	10.177	107%
B-af	Zn	141	4	0.056	0.030	4.149	105%
C-af	Zn	141	4	0.059	0.022	3.057	97%
A	Zn	141	4	0.053	0.027	3.642	95%
B	Zn	141	4	0.044	0.026	3.548	99%
C	Zn	141	4	0.042	0.017	2.303	96%
D-NP-ap	Zn	141	4	0.058	0.041	5.552	111%
D-AQ-ap	Zn	141	4	0.057	0.040	5.468	112%
D-ap	Zn	141	4	0.043	0.025	3.443	110%
D-NP	Zn	141	4	0.060	0.028	3.870	96%
D-AQ	Zn	141	4	0.062	0.033	4.532	96%
D	Zn	141	4	0.031	0.018	2.507	96%

230

231

Table S10: Contains the fractions from Cu EXAFS LCF displayed in Figure 2.

Sample	Sum	Cu _x S (amorphous)	CuS (covellite)	CuFeS ₂ (chalcopyrite)	CuO (tenorite)	CuSO ₄ (copper sulphate)	CuFe ₂ O ₄ (cuprospinel)	Cu(II)-acetate
A-ap	1.218	0.18	0.17	0.00	0.14	0.29	0.44	0.00
B-ap	0.98	0.28	0.00	0.00	0.28	0.36	0.06	0.00
C-ap	0.972	0.29	0.00	0.00	0.32	0.22	0.14	0.00
A-af	1.257	0.33	0.00	0.00	0.22	0.00	0.52	0.19

B-af	0.881	0.21	0.00	0.00	0.25	0.18	0.11	0.14
C-af	0.965	0.24	0.00	0.02	0.21	0.30	0.11	0.08
A	1.135	0.95	0.00	0.03	0.05	0.00	0.00	0.10
B	1.179	1.00	0.08	0.00	0.02	0.00	0.00	0.08
C	1.102	0.80	0.00	0.13	0.10	0.08	0.00	0.00
D-NP-ap	1.001	0.32	0.00	0.00	0.33	0.18	0.17	0.00
D-AQ-ap	0.999	0.29	0.00	0.02	0.31	0.19	0.18	0.00
D-ap	0.988	0.35	0.00	0.00	0.31	0.16	0.17	0.00
D-NP	1.231	1.00	0.00	0.13	0.08	0.02	0.00	0.00
D-AQ	1.181	1.00	0.00	0.18	0.00	0.00	0.00	0.00
D	1.29	1.00	0.00	0.29	0.00	0.00	0.00	0.00

232

233 Table S11: Contains the fractions from Zn EXAFS LCF displayed in Figure 3

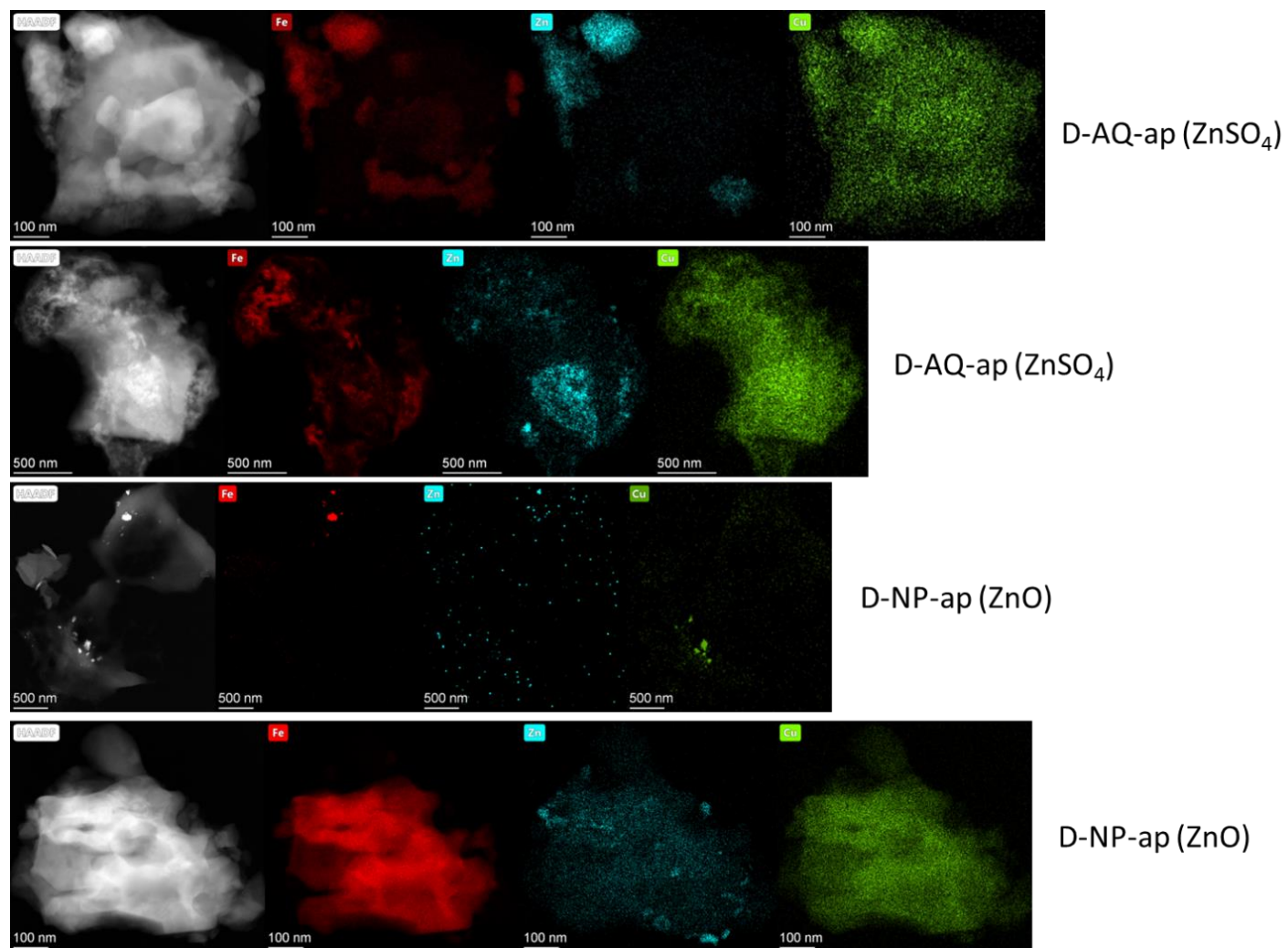
Sample	Sum	ZnS (sphalerite)	Zn Ferrihydrite CPT	ZnO (zincite)	ZnAl ₂ O ₄ (gahnite)
A-ap	1.074	0.00	0.68	0.00	0.37
B-ap	1.029	0.00	1.00	0.06	0.00
C-ap	1.029	0.00	1.00	0.02	0.00
A-af	1.065	0.00	0.68	0.03	0.37
B-af	1.048	0.00	0.85	0.02	0.19
C-af	0.969	0.00	0.89	0.09	0.00
A	0.946	0.64	0.27	0.09	0.00
B	0.986	0.71	0.21	0.08	0.00
C	0.963	0.47	0.46	0.08	0.00
D-NP-ap	1.109	0.00	1.00	0.00	0.20
D-AQ-ap	1.12	0.00	1.00	0.00	0.19
D-ap	1.095	0.00	1.00	0.00	0.15
D-NP	0.963	0.57	0.28	0.11	0.00
D-AQ	0.957	0.65	0.23	0.08	0.00
D	0.96	0.73	0.16	0.07	0.00

234

235

S10. Electron microscopy analysis of the sewage sludge ash

Selected ash samples (D-NP-ap (Zn), D-AQ-ap (Zn)) were investigated with a (scanning) transmission electron microscope (S)TEM (Talos F200X, Super-X EDS, 4 detector configuration, FEI, USA) at an accelerating voltage of 200 kV and the data was processed using the software Velox 2.8 (FEI, USA). High angle annular dark field (HAADF) images and elemental distribution maps are given in Figure S13.



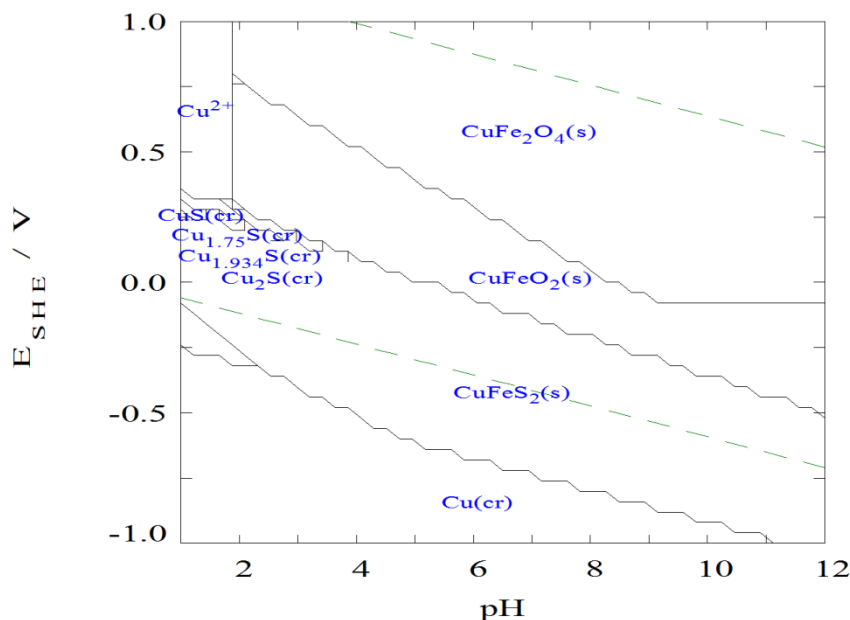
241

242 Figure S13: HAADF image (first images on the left) of selected ash grains of D-AQ-ap (ZnSO_4 , first two rows) and D-NP-ap (ZnO , last two rows).

243 Elemental distribution maps derived from EDX measurements are provided in colored maps (Fe, Zn, Cu from left to right).

244

S11. Thermodynamic equilibrium calculations

 $[\text{Fe}^{2+}]_{\text{TOT}} = 10.00 \text{ mM}$
 $I = 0.010 \text{ M}$
 $[\text{Cu}^{2+}]_{\text{TOT}} = 1.00 \text{ mM}$
 $[\text{HS}^-]_{\text{TOT}} = 2.60 \text{ mM}$

 $t = 25^\circ\text{C}$

245

Figure S14: Pourbaix diagram of Cu in the presence of Fe and S. The graph is created using MEDUSA and HYDRA¹⁹. Concentrations were chosen based on sludge collected at the WWTP Werdhoelzli.

248

References

1. Jakobsen, H. A., Fluidized Bed Reactors. In *Chemical Reactor Modeling*, Springer: Berlin, Heidelberg, 2009.
2. Yates, J. G.; Lettieri, P., Conversion of Biomass and Waste Fuels in Fluidized-Bed Reactors. In *Fluidized-Bed Reactors: Processes and Operating Conditions*, Springer International Publishing: Cham, 2016; pp 111-135.
3. Hagesaether, L.; Jakobsen, H. A.; Svendsen, H. F., Theoretical analysis of fluid particle collisions in turbulent flow. *Chemical Engineering Science* **1999**, *54* (21), 4749-4755.
4. Hagesaether, L.; Jakobsen, H. A.; Svendsen, H. F., Modeling of the Dispersed-Phase Size Distribution in Bubble Columns. *Industrial & Engineering Chemistry Research* **2002**, *41* (10), 2560-2570.
5. Heller, R.; McGannon, J.; Weber, A., Precision determination of the lattice constants of zinc oxide. *Journal of Applied Physics* **1950**, *21* (12), 1283-1284.
6. Prince, E.; Treuting, R. G., The structure of tetragonal copper ferrite. *Acta Crystallographica* **1956**, *9* (12), 1025-1028.
7. Tasca, J. E.; Quincoces, C. E.; Lavat, A.; Alvarez, A. M.; González, M. G., Preparation and characterization of CuFe₂O₄ bulk catalysts. *Ceramics International* **2011**, *37* (3), 803-812.

8. Jacquat, O.; Voegelin, A.; Juillot, F.; Kretzschmar, R., Changes in Zn speciation during soil formation from Zn-rich limestones. *Geochimica et Cosmochimica Acta* **2009**, 73 (19), 5554-5571.
9. Cornell, R. M.; Schwertmann, U., *The iron oxides: structure, properties, reactions, occurrences and uses*. John Wiley & Sons: 2003.
10. Ravel, B.; Newville, M., ATHENA, ARTEMIS, HEPHAESTUS: data analysis for X-ray absorption spectroscopy using IFEFFIT. *Journal of Synchrotron Radiation* **2005**, 12 (4), 537-541.
11. Gualtieri, A. F.; Venturelli, P., In situ study of the goethite-hematite phase transformation by real time synchrotron powder diffraction. *American Mineralogist* **1999**, 84 (5-6), 895-904.
12. Nilsen, M. H.; Nordhei, C.; Ramstad, A. L.; Nicholson, D. G.; Poliakoff, M.; Cabañas, A., XAS (XANES and EXAFS) Investigations of Nanoparticulate Ferrites Synthesized Continuously in Near Critical and Supercritical Water. *The Journal of Physical Chemistry C* **2007**, 111 (17), 6252-6262.
13. Whitaker, A., The crystal structure of hopeite, $\text{Zn}_3(\text{PO}_4)_2 \cdot 2.4 \text{H}_2\text{O}$. *Acta Crystallographica Section B: Structural Crystallography and Crystal Chemistry* **1975**, 31 (8), 2026-2035.
14. Werther, J.; Ogada, T., Sewage sludge combustion. *Progress in Energy and Combustion Science* **1999**, 25 (1), 55-116.
15. Malinowski, E. R., *Factor analysis in chemistry*. Wiley: 2002.
16. Patrick, R. A. D.; Mosselmans, J. F. W.; Charnock, J. M.; England, K. E. R.; Helz, G. R.; Garner, C. D.; Vaughan, D. J., The structure of amorphous copper sulfide precipitates: An X-ray absorption study. *Geochimica et Cosmochimica Acta* **1997**, 61 (10), 2023-2036.
17. Malinowski, E. R., Theory of error for target factor analysis with applications to mass spectrometry and nuclear magnetic resonance spectrometry. *Analytica Chimica Acta* **1978**, 103 (4), 339-354.
18. Webb, S. M., SIXpack: a graphical user interface for XAS analysis using IFEFFIT. *Physica Scripta* **2005**, 2005 (T115), 1011.
19. Puigdomenech, I., Hydra/Medusa chemical equilibrium database and plotting software. *KTH Royal Institute of Technology* **2004**.